Flame propagation in two-dimensional solids: Particle-resolved studies with complex plasmas

S. O. Yurchenko,[1,*] E. V. Yakovlev,[1] L. Couëdel,[2] N. P. Kryuchkov,[1] A. M. Lipaev,[3] V. N. Naumkin,[3] A. Yu. Kislov,[1] P. V. Ovcharov,[1] K. I. Zaytsev,[1] E. V. Vorob'ev,[1] G. E. Morfill,[1,4] and A. V. Ivlev[4,†]

[1]*Bauman Moscow State Technical University, 2nd Baumanskaya Street 5/1, 105005 Moscow, Russia*

[2]*CNRS, Aix Marseille Université, PIIM, UMR 7345, 13397 Marseille, France*

[3]*Joint Institute for High Temperatures, 125412 Moscow, Russia*

[4]*Max-Planck-Institut für Extraterrestrische Physik, Giessenbachstrasse 1, 85748 Garching, Germany*

(Received 17 May 2017; published 2 October 2017)

Using two-dimensional (2D) complex plasmas as an experimental model system, particle-resolved studies of flame propagation in classical 2D solids are carried out. Combining experiments, theory, and molecular dynamics simulations, we demonstrate that the mode-coupling instability operating in 2D complex plasmas reveals all essential features of combustion, such as an activated heat release, two-zone structure of the self-similar temperature profile ("flame front"), as well as thermal expansion of the medium and temperature saturation behind the front. The presented results are of relevance for various fields ranging from combustion and thermochemistry, to chemical physics and synthesis of materials.

DOI: 10.1103/PhysRevE.96.043201

I. INTRODUCTION

Flame is a complex phenomenon of a very broad interest, occurring in gases, liquids, or solids. In the most simple representation, flames are characterized by Arrhenius-like activation of exothermic chemical reactions, with the main mechanism of heat transfer from the flame front being ordinary conductivity [1,2]. Generally, propagation of the combustion is governed by the kinetics of chemical reactions and thermodynamics of the medium. Different regimes can be observed—in particular, flames in a given medium can be much slower than sound (slow combustion), or they can propagate at supersonic velocities (see, e.g., Refs. [3–5]).

The interest in combustion and flames in solids is stimulated by numerous fundamental and applied problems. Among them are high-temperature synthesis of materials [6], laser-induced thermochemical reactions [7], and development of solid fuels and reactive media [8–11]. Study of flames in reactive solids is also important for astrophysics and astrochemistry [12], since the leading mechanism of desorption of icy mantles covering cosmic dust may be their chemical explosion (triggered in the chemically rich mantles by collisions with cosmic rays). Apart from the systems with chemical reactivity, combustionlike phenomena were recently observed [13,14] in explosive relaxation of molecular magnets, including magnetic systems with pulsating and detonationlike behavior [15–17]. Combustion has also been studied numerically by employing the reactive molecular dynamic simulations (see, e.g., Refs. [18–21]). However, to the best of our knowledge, experimental particle-resolved studies of flames in solids have never been carried out.

In this paper, we present particle-resolved studies of flames in two-dimensional (2D) solids. Monolayer plasma crystals are used as a model system for this purpose, where the mode-coupling instability (MCI) operating in the crystalline and fluid regimes is employed to mimic ignition and activation of the medium in the propagating flame fronts. Using our experiments, molecular dynamic simulations, and proposed theory, we demonstrate the physical analogy between the developed MCI in 2D complex plasmas and flame fronts in regular solids. The results open novel prospects in studies of flame fronts, their structure, local dynamics, and related phenomena in reactive solids and soft matter.

II. MOTIVATION

2D complex (dusty) plasmas are known to be a convenient experimental model system, where various generic phenomena occurring in classical liquids and solids can be studied at the most fundamental, particle-resolved level [22,23]. Typically, experiments with 2D complex plasmas are performed in a rf argon discharge; negatively charged monodisperse microparticles levitate over a flat rf electrode due to the balance of gravitational and electrostatic forces, and can be directly imaged from above with a video camera. For a sufficiently strong vertical confinement and/or low areal number density, the system of charged microparticles can be described by an effective Hamiltonian, which has been utilized for studying melting and crystallization [24–29], diffusion [30,31], heat transfer [32,33], and plastic deformations [34–36].

On the other hand, a broad range of nonequilibrium phenomena can be observed in 2D complex plasmas [37,38], since the interactions between microparticles are affected by the vertical plasma flow, generating the so-called "plasma wakes" downstream from each particle [39–41]. Such interparticle forces violate the action-reaction symmetry [37], and their magnitude can be tuned by changing experimental parameters [42]. Therefore, 2D complex plasmas serve a thermodynamically open system with tunable interactions [38], where microparticles can efficiently acquire energy from the surrounding flowing plasma.

The nonreciprocal wake-mediated interactions can trigger the MCI both in crystalline [43–45] and fluid [46,47] complex plasmas. A necessary condition of the instability onset is a crossing of the out-of-plane and (longitudinal) in-plane wave modes, leading to the formation of the unstable hybrid mode

*st.yurchenko@mail.ru
†ivlev@mpe.mpg.de

and a rapid increase of the particles' kinetic energy. In crystals, the modes cross only when the number density of particles in a monolayer exceeds a certain threshold, and therefore the MCI normally starts in the central, densest region, provided the vertical confinement is sufficiently weak [32,45]. From a practical viewpoint, this is the easiest way to melt a 2D plasma crystal. On the contrary, the wave modes in a fluid monolayer always cross; hence, the fluid MCI has no density or confinement threshold and can operate under conditions where a crystalline monolayer is stable [46]. This latter mechanism of the heating activation in an otherwise stable monolayer provides a direct analogy with the activation in conventional reactive media.

III. EXPERIMENTAL

To explore the analogy between the MCI-induced melting and the flame propagation, we performed dedicated experiments. These were carried out in a modified gaseous electronics conference (GEC) chamber, in a capacitively coupled rf glow discharge at 13.56 MHz, where the top electrode is a grounded ring and the powered bottom electrode is an aluminum disk with a diameter of $\simeq 220$ mm. The argon gas pressure and the forward rf power were controlled in the range of 0.5–2.5 Pa and 5–20 W, respectively. Melamine-formaldehyde microspheres of the diameter 9.19 ± 0.14 μm and mass $m = 6.1 \times 10^{-10}$ g were injected in the discharge. They acquired large negative charges and became confined in the sheath above the rf electrode. Heavy agglomerates were removed, and 2D plasma crystals with diameter about 100 mm were formed. Further details about the experimental setup can be found in Refs. [48] and [47]. For similar experiments, see Refs. [49], [45], and [47].

The microparticles were illuminated by a horizontal laser sheet and imaged through a window at the top of the chamber by a Photron FASTCAM SA6 camera at 250 frames per second. (An additional side-view camera Edmund Optics 0413M was used to verify that the microparticles formed a single layer.) To obtain the particle coordinates and velocities in each frame, we used the standard approach [50,51]. The structures were analyzed by performing the Voronoi triangulation, and the bond-orientational order parameter Ψ_6 was calculated for each cell,

$$\Psi_6 = \frac{1}{N_{\rm nn}} \sum_{j=1}^{N_{\rm nn}} e^{6i\theta_j},$$

where $N_{\rm nn}$ is the number of the nearest neighbors and θ_j is the bond angle for the jth neighbor. Furthermore, to evaluate the kinetic temperature of particles, i.e., the thermal part of particle kinetic energy, the collective motion (associated with the acoustic fluctuations) was subtracted from the velocity field:

$$T = \frac{m}{2} \sum_i (\mathbf{v}_i - \langle \mathbf{v}_i \rangle)^2,$$

where $\mathbf{v}_i$ is the instantaneous in-plane velocity of the ith particle, and $\langle \mathbf{v}_i \rangle$ is the instantaneous average velocity of all particles in the vicinity of radius $2.4a$ around the ith particle.

The crystalline MCI was studied at a pressure of 1 Pa and rf power 20 W. Under these conditions the MCI, triggered in the central region, was expanding outward. Eight experiments were performed in total, providing quite similar results. Here, we present detailed analysis of one of them, completely illustrating their common features. Onset and development of the instability in this experiment can be seen in Movie S1 of the Supplemental Material [52].

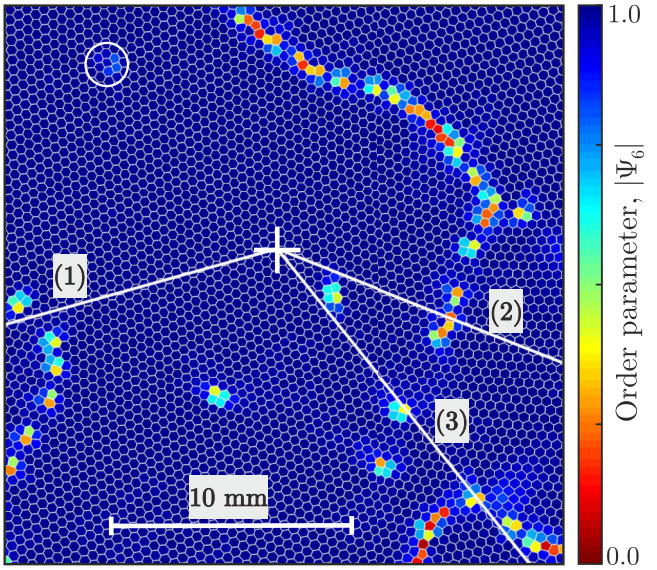

FIG. 1. Example of a stable 2D plasma crystal observed in experiments (top view). The Voronoi cells are color-coded, representing the magnitude of the bond-orientational order parameter Ψ_6. The numbered straight lines mark the analyzed radial directions of MCI propagation.

Figure 1 shows the central area of a stable crystal (before the MCI onset) and the analyzed radial directions of the propagation. The mean interparticle distance (lattice constant) in the center was $a = 390 \pm 25$ μm. Three directions were chosen for the analysis: Directions (1) and (2) are almost without dislocations, while direction (3) crosses a dislocation line. Note that in the left upper quarter of the figure, one can see a single active particle (marked by the ring). We found that the particle only weakly affects the background temperature in its vicinity.

Figure 2 demonstrates evolution of the kinetic temperature. Upon reduction of the vertical confinement (achieved by a slight decrease of the rf discharge power) below the threshold, the unstable hybrid mode is formed [see Fig. 7(b) in Appendix A] and the crystalline MCI sets in; the kinetic energy in the central region rapidly increases and the crystal melts. Then, the melting expands outward in a form of a sharp front, completely destroying the entire crystal. The steady front propagation is sustained by efficient heating due to the fluid MCI, so the kinetic temperature behind the front exceeds that in the crystalline region by about 3 orders of magnitude.

Figure 3 shows the formation of the flame front. The oscillating horizontal stripes seen at the initial (ignition) phase are a typical fingerprint of the crystalline MCI [32]. The initial melting rapidly develops into a hot zone with a steady front, propagating outward at a constant radial velocity of $v_{\rm fr} = 7.0 \pm 0.2$ mm/s. We point out that the steady hot-zone expansion occurs at the periphery of the crystalline monolayer, where the equilibrium particle density is noticeably (by $\simeq$

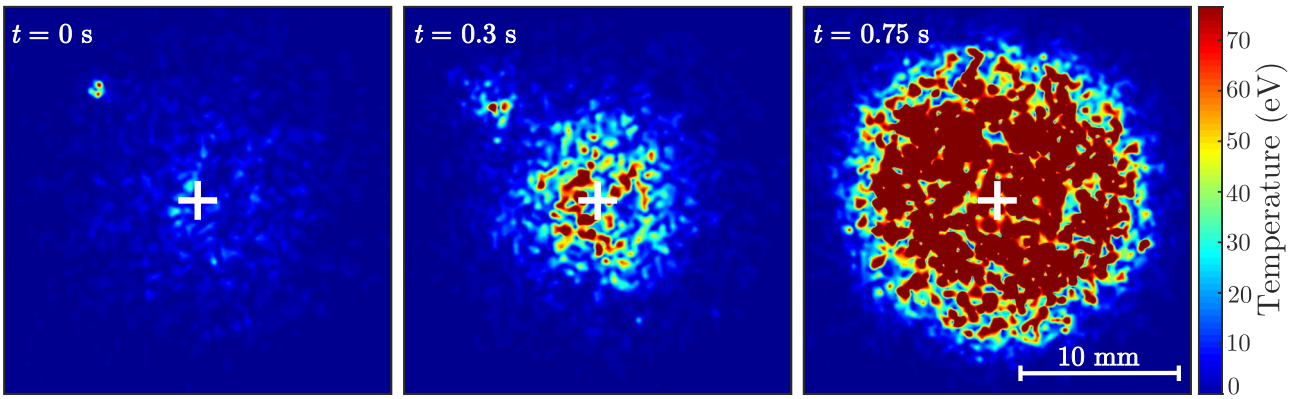

FIG. 2. Typical evolution of the kinetic temperature of particles in a 2D plasma crystal (top view). The crystalline MCI triggers melting of the central region, then the melting expands outward in the form of a sharp front, supported by intense heating behind the front due to the fluid MCI; see also Movie S1 [52].

25%) lower than in the center and therefore no crystalline MCI can be maintained. This clearly indicates activation of the fluid MCI occurring near the front. We also note that, apart from the crystalline MCI, the ignition can be realized by other means, e.g., by a local laser heating or by a rapidly moving particle [53].

IV. MOLECULAR DYNAMICS SIMULATIONS

Complementing the experiments, we carried out molecular dynamics (MD) simulations (see Appendix B for details). Figure 4 illustrates modification of the wave modes upon melting, as obtained from the simulations. In a stable crystalline state, the particle fluctuation spectra remain practically unchanged up to the melting point (where T_m is the equilibrium melting temperature). Right after melting, the modes start changing rapidly—the out-of-plane and in-plane modes merge, as one can see by comparing panels (a) and (b), thus approaching conditions for the onset of fluid MCI. Simulations demonstrate that the hybrid mode is formed at a certain "activation" temperature T_*, corresponding to a significant loss of interparticle correlations (typically, T_* is several time higher than T_m). Movie S2 [52], representing MD simulations for the conditions of experiments (Figs. 1–3), shows striking similarity with experimental Movie S1. It is noteworthy that an excellent agreement between experiment and simulations is also revealed in terms of the quantitative analysis presented below.

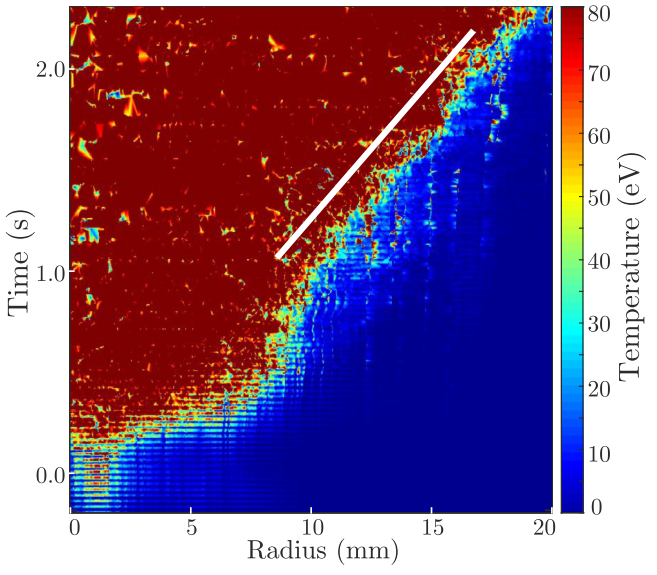

FIG. 3. Radial expansion of the hot zone with time [for the radial direction (1) in Fig. 1]. One can see the ignition phase due to the crystalline MCI, crossing over (at $t \simeq 1$ s) to a steady expansion sustained due to the fluid MCI (marked by the white solid line).

V. ANALYSIS AND DISCUSSION

To highlight the principal analogy between propagation of the flame fronts and the MCI-induced melting, we consider evolution of the spatial temperature distribution $T(r,t)$ in a continuous reactive medium, described by the following heat equation [2]:

$$\frac{\partial T}{\partial t} = \frac{Q(T)}{Cn} + \chi\left(\frac{\partial^2 T}{\partial r^2} + \frac{D-1}{r}\frac{\partial T}{\partial r}\right), \qquad (1)$$

where $Q(T)$ is the reaction heat rate of the medium (of the spatial dimension D), χ is the thermal diffusivity, n is the number density, and C is the isobaric heat capacity per particle. In a steady front regime, the second term in the parentheses becomes asymptotically small, and therefore the explicit effect of dimensionality vanishes as well.

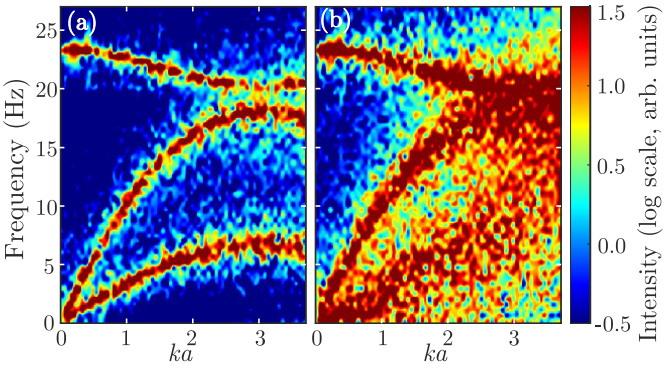

FIG. 4. Particle fluctuation spectra (MD simulations): (a) a crystal ($T/T_m \simeq 0.9$) where the out-of-plane and in-plane modes do not cross, and (b) how the modes merge after melting ($T/T_m \simeq 1.3$).

The heat source $Q(T)$ is determined by the chemical kinetics in a given reactive medium; e.g., $Q(T) \propto \exp(-E_A/T)$ for the Arrhenius-like chemical activation, with E_A being the activation energy. Generally, $Q(T)$ can be a complex function of temperature, and its particular features may be important for critical heat phenomena, such as ignition and heat explosion [1]. On the contrary, for a steady flame propagation these features are of minor importance, since the temperature changes rapidly across the front. In this case, the main role is played by the behavior of $Q(T)$ at low and high temperatures. For this reason, in the theory of combustion and flame $Q(T)$ is routinely approximated by the Heaviside step function [1].

Thus, to describe the heat source for the fluid MCI we can use

$$\frac{Q(T)}{Cn} = \begin{cases} 0, & T < T_*; \\ q_\infty, & T > T_*, \end{cases} \tag{2}$$

where T_* is the activation temperature at which the unstable hybrid mode forms, triggering the fluid MCI. The maximum heating is estimated as $q_\infty \approx \gamma(T_\infty)T_\infty/C$, where $T_\infty \approx 1$ keV is the saturation temperature of the fluid MCI [46] and $\gamma(T)$ is the (temperature-dependent) growth rate of the instability. We note that unlike "true" 2D systems, the heat capacity of 2D fluid complex plasmas varies in the range of $C = 2$–3, since the vertical confinement has a finite strength and, hence, the vertical motion may provide a substantial contribution to C [54].

The self-similar temperature profile across a steady flame front, governed by Eqs. (1) and (2), has the following form [12]:

$$\frac{T(\tau) - T_0}{T_* - T_0} = \begin{cases} \exp\left(\tau v_{fr}^2/\chi\right), & \tau < 0; \\ 1 + \tau v_{fr}^2/\chi, & \tau > 0, \end{cases} \tag{3}$$

where $\tau = t - r/v_{fr}$ is the self-similar time and v_{fr} is the front velocity, related to the activation temperature via $T_* - T_0 = q_\infty \chi / v_{fr}^2$. Regimes $\tau \lessgtr 0$ represent, respectively, a nonactivated crystalline state preheated by thermal diffusion and a state with developed fluid MCI; for classical flames, these two regimes correspond to the *inert* and *reactive zones* [1].

Heat balance in complex plasmas is generally affected by the interaction of microparticles with neutral gas. This leads to the appearance of an additional term $-2\gamma_d(T - T_0)/C$ on the right-hand side of Eq. (1), where T_0 is the equilibrium temperature in the absence of heating and γ_d is the Epstein damping rate (for our experimental conditions, $\gamma_d \simeq 1.2\ \mathrm{s}^{-1}$). However, as shown in Appendix C, the damping can be neglected if the growth rate v_{fr}^2/χ is much larger than $2\gamma_d/C$; the analysis below confirms that this condition is well fulfilled for our experiments.

To obtain the experimental self-similar profile $T(\tau)$, we averaged the thermal part of the particle kinetic energy at different radial distances from the hot-zone center (see Sec. III). We also calculated the fraction of sixfold Voronoi cells, $c_6(\tau)$, to identify the melting onset. The results are presented in Fig. 5. The equilibrium temperature $T_0 = 70 \pm 40$ meV was derived by averaging the temperature points far from the front, at $\tau \lesssim -2.5$ s in Fig. 5, and the fit to Eq. (3) (solid line) was then obtained by using the least-squares

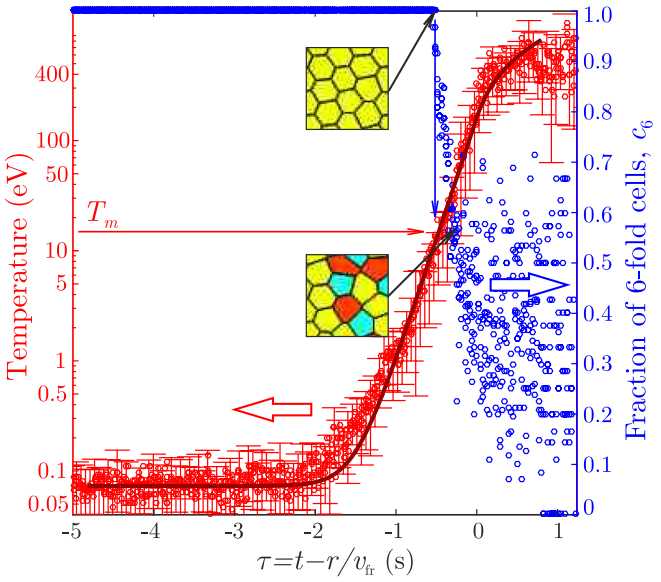

FIG. 5. Self-similar profiles of the particle kinetic temperature $T(\tau)$ (left axis) and of the fraction of sixfold cells $c_6(\tau)$ (right axis). The symbols are experimental results, and the solid line is a fit to Eq. (3). The insets demonstrate color-coded snapshots of the Voronoi diagram near the flame front: sixfold cells are yellow, while five- and sevenfold cells are blue and red, respectively.

method with varying activation temperature T_*, growth rate v_{fr}^2/χ, and position of the activation point $\tau = 0$. This yields $T_* = 160 \pm 15$ eV and $v_{fr}^2/\chi = 5.1 \pm 0.1\ \mathrm{s}^{-1}$; from the latter we derive $\chi \simeq 9.6\ \mathrm{mm}^2/\mathrm{s}$, which reasonably agrees with previous measurements of the thermal diffusivity [33].

Figure 5 demonstrates an excellent agreement between the experimental and theoretical temperature profiles. The temperature grows exponentially in the crystal, where c_6 is equal to unity; the melting sets in when c_6 starts decreasing abruptly, as illustrated by the two snapshots of the Voronoi diagram. One can see that the melting occurs at $\simeq 14$ eV, which coincides with the equilibrium melting temperature T_m for a 2D Yukawa crystal [55,56], calculated for the experimental values of the screening parameter and the particle charge (see Appendix A). Analysis performed for other radial directions yields practically the same results (see Appendix D).

According to Fig. 4, the mode crossing starts at temperatures slightly above T_m, but in order to achieve the activation (i.e., to provide optimum conditions for the fluid MCI) the interparticle correlations should be largely destroyed [46]. This requires significant overheat of the inert zone and, therefore, the activation temperature T_* occurs to be much larger than T_m, as follows from Fig. 5 (and also from our MD simulations).

In the reactive zone $T > T_*$ ($\tau > 0$), a temperature plateau gradually builds up. The main physical reason for that is a substantial isobaric expansion of strongly heated fluids. While the thermal expansion further contributes to the loss of correlations and thus stimulates activation of the fluid MCI, the instability naturally saturates when the density decreases [46]. Figure 6 demonstrates a comparison between the experimental and theoretical self-similar profiles of the areal density, $n(\tau)$. The theoretical curve $n(\tau)$ was obtained for a constant pressure (at the melting point) from the thermodynamic data [56], using

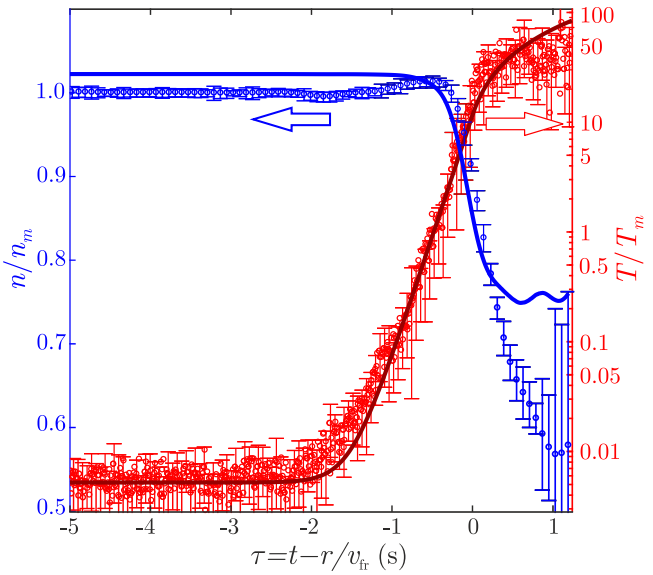

FIG. 6. Comparison between experimental (blue symbols) and theoretical (blue solid line) self-similar profiles of the particle density $n(\tau)$. The red symbols and the solid line represent the same self-similar temperature profile $T(\tau)$ as in Fig. 5. The theoretical curve $n(\tau)$ shows the equilibrium density of a 2D Yukawa system, calculated for the experimentally measured $T(\tau)$. The density and temperature are normalized by the respective values at the melting point.

the screening length $\lambda = a/\kappa$ deduced from the experiment (see Appendix A). A small time shift between the experimental and theoretical density profiles, due to a finite velocity of the front, is estimated as $2.4a/v_{fr} \simeq 0.15$ s. Otherwise, we see a remarkable agreement, suggesting that the density drop seen up to $\tau \approx 0.3$ s is due to the isobaric expansion of the heated fluid. Note that at later times, the vertical confinement cannot keep the most energetic particles in the illuminated field of view, which causes a further (apparent) decrease of the density.

The maximum heating q_∞, which controls the propagation velocity v_{fr}, is proportional to the growth rate of the saturated MCI, $\gamma(T_\infty)$. As discussed above, the latter is determined by a competition between the MCI activation and the thermal expansion in the reactive zone. This is fully analogous to chemically reactive media, where the heating and thermal expansion also occur simultaneously. Furthermore, the thermal equilibrium is achieved at the saturation temperature T_∞, where the heating due to fluid MCI is balanced by frictional dissipation, $\gamma(T_\infty) \simeq 2\gamma_d$. This latter can be utilized in the future to form a *homogeneous fluid* 2D complex plasma with controllable temperature.

We point out that preheating of the inert zone is due to the thermal diffusivity, primarily conducted by longitudinal (compressional wave) phonons [33] whose velocity C_l is typically much larger than the velocity of transversal (shear wave) phonons C_t. In our experiment, the velocity of the flame front $v_{fr} = 7.0 \pm 0.2$ mm^2/s is much smaller than $C_l = 32.4 \pm 3.8$ mm/s but is very close to $C_t = 7.3 \pm 0.9$ mm/s (see Appendix A). Thus, the front is almost sonic with respect to the shear waves participating in the elastic relaxation of the system. We are not aware of any dedicated studies of sonic flames in solids, which should be an interesting topic for a separate work.

VI. CONCLUSIONS

The presented results pave the way for particle-resolved studies of a variety of problems. Examples include flames in reactive media with different mechanisms of activation, structure of preheated zones in crystals, dependence of the propagation velocity on the heating rate, role of lattice deformations and defects, transition between slow and supersonic regimes of the flame propagation, identification of the generic microscopic processes governing combustion in solids, etc. We believe that our results will be useful for related areas of chemical physics, material sciences, astrophysics and astrochemistry, and soft condensed matter.

ACKNOWLEDGMENTS

The authors are grateful to Dr. Alexei D. Kiverin for useful discussions. The experimental study is supported by Russian Science Foundation (RSF) Grant No. 14-43-00053; postprocessing is supported by Russian Foundation for Basic Research through Grant No. 16-38-00952; and MD simulations of the flame front propagation are supported by RSF Grant No. 17-19-01691.

APPENDIX A: FLUCTUATION SPECTRA

Figure 7 presents the experimentally measured fluctuation spectra, obtained before the onset of the crystalline MCI. Then the spectra were calculated by applying the Fourier transform to the particle currents in the same way as reported in Ref. [47]. Then the spectra were fitted by the theoretical dispersion relations [44,45]. From this, we evaluated the particle charge $Q = -(20 \pm 0.5) \times 10^3 e$ (e is the elementary charge) and the screening parameter $\kappa = a/\lambda = 1.2 \pm 0.1$ (λ is the effective screening length of the pair interactions). The longitudinal and transversal wave velocities $C_l = 32.4 \pm 3.8$ mm/s and $C_t = 7.3 \pm 0.9$ mm/s, respectively, were calculated from the slopes of the in-plane dispersion relations at $k \to 0$.

APPENDIX B: DETAILS OF MD SIMULATIONS

The fluctuation spectra shown in Fig. 4 were deduced from MD simulations, where particles interact via the Yukawa (Debye-Hückel) potential $\varphi(r) = (Q^2/r)\exp(-r/\lambda)$, with the effective screening length λ which determines the screening parameter $\kappa = (S/\pi N\lambda^2)^{1/2}$ (here, $N/S = n$ is the areal density). The system was placed into the vertical parabolic potential well $U(z) = \frac{1}{2}m\Omega^2 z^2$, where Ω is the frequency of the out-of-plane particle oscillations in the limit $k \to 0$. The value of Ω was derived from the experimental fluctuation spectra shown in Fig. 7.

The simulations were performed in the NVT ensemble using $N = 10^4$ particles and the Langevin thermostat. The numerical time step of $\Delta t = 5 \times 10^{-3}\sqrt{m\lambda^3/Q^2}$ was chosen, and the cutoff radius of the potential was set equal to $15(S/N)^{1/2}$. Simulations for $\kappa = 1.2$ were run for 10^5 time steps to equilibrate the system. Then the fluctuation spectra were calculated in the same manner as for our experimental data shown in Fig. 7.

To simulate the flame propagation, we took into account the plasma wakes. The interparticle interactions in

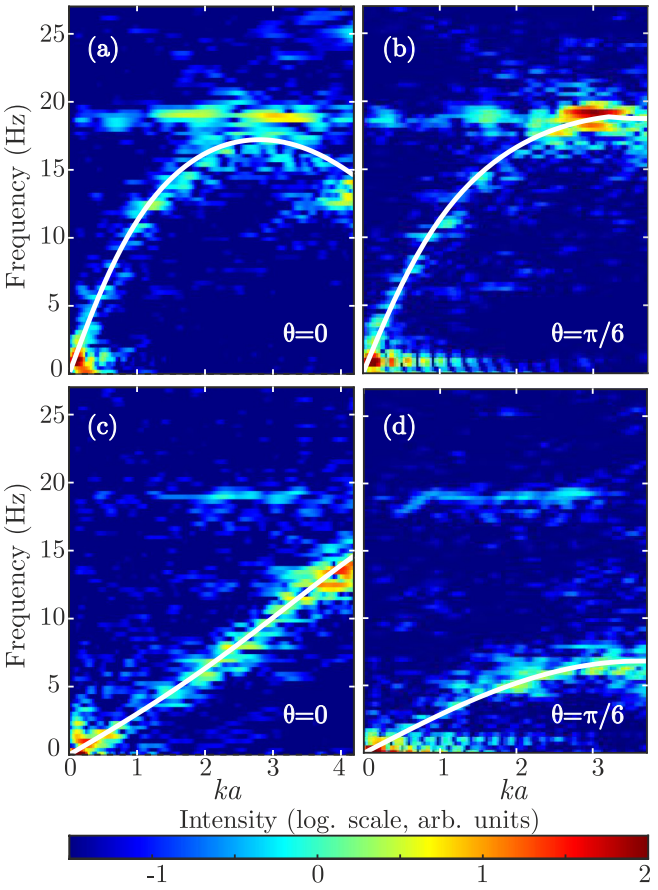

FIG. 7. Experimentally measured fluctuation spectra in the central region of a 2D plasma crystal. Shown are the in-plane longitudinal (a, b) and transversal (c, d) wave modes propagating along the principal lattice axes; the angle θ is between the wave vector and the nearest-neighbor director of the triangular lattice. The white solid lines are fits with the theoretical dispersion relations [44].

this case were described by a simple point-wake model (e.g., Refs. [45] and [44]):

$$\varphi(r) = Q^2\left[\frac{e^{-r/\lambda}}{r} - q\frac{e^{-r_w/\lambda}}{r_w}\left(1 + b\frac{e^{-r_w/\lambda}}{r_w/\lambda}\right)^{-1}\right],$$

where q is the relative wake charge, $r_w = |\mathbf{r} + h\mathbf{e}_z|$ is the distance to the wake of a neighboring particle, and h is the effective wake length. We choose the following wake parameters [47]: $q = 0.3, h = 0.3a$, and introduced the dimensionless cutoff $b = 0.1$ to truncate artificial divergence of the particle-wake interactions (peculiar to this toy model).

The particles were placed into the potential well $U(\mathbf{r}) = \frac{1}{2}m\Omega^2[z^2 + \alpha(x^2 + y^2)]$, with $\alpha = 2 \times 10^{-5}$ accounting for a weak horizontal confinement. The simulations were performed in the NVT ensemble for $N = 4 \times 10^4$ particles and the Langevin thermostat with the equilibrium temperature T_0. We set $T_0 = 60$ meV and used the screening parameter $\kappa = 1.2$ and the damping rate $\gamma_d = 1.2$ s^{-1}, as estimated from the experiment.

In Movie S2 of the Supplemental Material [52] we demonstrate the ignition phase and the transition to steady flame propagation, as seen in the simulation. Note that the

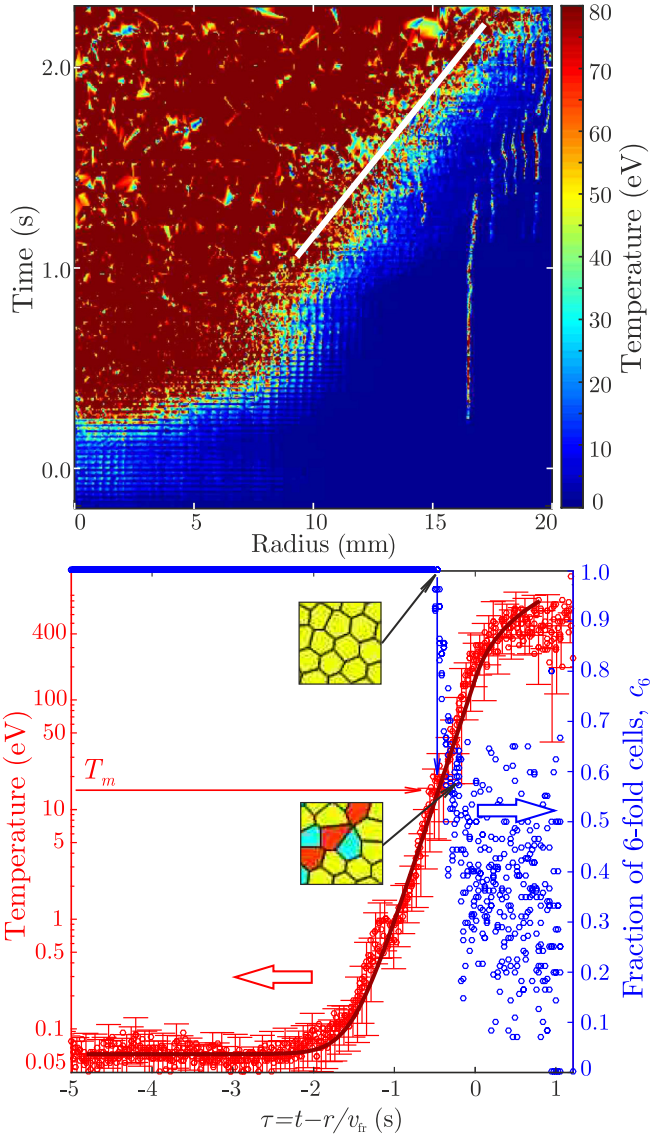

FIG. 8. Legends for the upper and lower panels are the same as for Figs. 3 and 5, respectively. The shown results are for the radial direction (3) in Fig. 1, and the fit parameters are $v_{fr} \simeq 7.0 \pm 0.2$ mm/s, $T_0 = 60 \pm 20$ meV, $T_* = 160 \pm 15$ eV, $v_{fr}^2/\chi = 5.1 \pm 0.1$ s^{-1}.

saturation temperature is about the experimentally observed value of $T_\infty \approx 1$ keV.

APPENDIX C: EFFECT OF DAMPING IN EQ. (1)

The heat equation, including the damping term, has the following form:

$$\frac{\partial T}{\partial t} = \frac{Q(T)}{Cn} - \frac{2\gamma_d}{C}(T - T_0) + \chi\frac{\partial^2 T}{\partial r^2}. \qquad \text{(C1)}$$

The self-similar temperature profile $T(t - r/v_{fr}) \equiv T(\tau)$ and its derivative should be continuous at the activation point ($\tau = 0$), where $T = T_*$. The resulting solution of Eq. (C1) is

$$\frac{T(\tau) - T_0}{T_* - T_0} = \begin{cases} e^{\lambda_1\tau}, & \tau < 0; \\ 1 + (1 - e^{-\lambda_2\tau})\lambda_1/\lambda_2, & \tau > 0, \end{cases} \qquad \text{(C2)}$$

where

$$\lambda_{1,2} = \left(\sqrt{1 + 8\gamma_d \chi / C v_{\rm fr}^2} \pm 1\right) v_{\rm fr}^2 / 2\chi$$

and

$$T_* - T_0 = \frac{q_\infty C}{2\gamma_d}\left(1 + \frac{\lambda_1}{\lambda_2}\right)^{-1}.$$

One can see that a finite damping introduces the temperature saturation at $T_\infty = q_\infty C/2\gamma_d$, where the heating through the fluid MCI is dissipated by friction.

For a weak damping, $\gamma_d \chi / C v_{\rm fr}^2 \ll 1$, we have $\lambda_1 \simeq v_{\rm fr}^2/\chi + 2\gamma_d/C$ and $\lambda_2 \simeq 2\gamma_d/C$. In this case, $e^{-\lambda_2 \tau}$ in Eq. (C2) can be expanded in a series, which yields Eq. (3).

APPENDIX D: DIRECTIONS OF PROPAGATION IN FIG. 1

The results obtained for directions (1) and (2) almost coincide; typical evolution of T for direction (1) is presented in Figs. 3 and 5. To demonstrate that dislocations do not affect the main features of the flame front, in Fig. 8 we also show the results for direction (3).

[1] Y. B. Zeldovich, G. I. Barenblatt, V. B. Librovic, and G. M. Makhviladze, *The Mathematical Theory of Combustion and Explosion* (Consultants Bureau, New York, 1985).

[2] L. D. Landau and E. M. Lifshitz, *Fluid Mechanics*, 2nd ed. (Elsevier, Oxford, 1987), Vol. 6.

[3] V. Alekseev, M. Kuznetsov, Y. Yankin, and S. Dorofeev, J. Loss Prev. Process Ind. **14**, 591 (2001).

[4] M. Kellenberger and G. Ciccarelli, Proc. Combust. Inst. **35**, 2109 (2015).

[5] A. Kiverin, I. Yakovenko, and M. Ivanov, Int. J. Hydrogen Energy **41**, 22465 (2016).

[6] A. G. Merzhanov and E. N. Rumanov, Rev. Mod. Phys. **71**, 1173 (1999).

[7] F. V. Bunkin, N. A. Kirichenko, and B. S. Lukyanchuk, Usp. Fiz. Nauk **138**, 45 (1982).

[8] M. B. Toftegaard, J. Brix, P. A. Jensen, P. Glarborg, and A. D. Jensen, Prog. Energy Combust. Sci. **36**, 581 (2010).

[9] V. V. Bychkov and M. A. Liberman, Phys. Rev. Lett. **73**, 1998 (1994).

[10] J. Maunuksela, M. Myllys, O.-P. Kähkönen, J. Timonen, N. Provatas, M. J. Alava, and T. Ala-Nissila, Phys. Rev. Lett. **79**, 1515 (1997).

[11] O. Zik, Z. Olami, and E. Moses, Phys. Rev. Lett. **81**, 3868 (1998).

[12] A. V. Ivlev, T. B. Röcker, A. Vasyunin, and P. Caselli, Astrophys. J. Lett. **805**, 59 (2015).

[13] Y. Suzuki, M. P. Sarachik, E. M. Chudnovsky, S. McHugh, R. Gonzalez-Rubio, N. Avraham, Y. Myasoedov, E. Zeldov, H. Shtrikman, N. E. Chakov, and G. Christou, Phys. Rev. Lett. **95**, 147201 (2005).

[14] D. A. Garanin and E. M. Chudnovsky, Phys. Rev. B **76**, 054410 (2007).

[15] M. Modestov, V. Bychkov, and M. Marklund, Phys. Rev. B **83**, 214417 (2011).

[16] M. Modestov, V. Bychkov, and M. Marklund, Phys. Rev. Lett. **107**, 207208 (2011).

[17] D. A. Garanin and S. Shoyeb, Phys. Rev. B **85**, 094403 (2012).

[18] Q.-D. Wang, J.-B. Wang, J.-Q. Li, N.-X. Tan, and X.-Y. Li, Combust. Flame **158**, 217 (2011).

[19] B. Saha, S. Shindo, S. Irle, and K. Morokuma, ACS Nano **3**, 2241 (2009).

[20] M. R. Weismiller, A. C. T. van Duin, J. Lee, and R. A. Yetter, J. Phys. Chem. A **114**, 5485 (2010).

[21] H.-J. Qian, A. C. T. van Duin, K. Morokuma, and S. Irle, J. Chem. Theory Comput. **7**, 2040 (2011).

[22] A. Ivlev, H. Löwen, G. Morfill, and C. P. Royall, *Complex Plasmas and Colloidal Dispersions: Particle-Resolved Studies of Classical Liquids and Solids* (Word Scientific, Singapore, 2012).

[23] G. E. Morfill and A. V. Ivlev, Rev. Mod. Phys. **81**, 1353 (2009).

[24] V. A. Schweigert, I. V. Schweigert, A. Melzer, A. Homann, and A. Piel, Phys. Rev. Lett. **80**, 5345 (1998).

[25] C.-L. Chan, W.-Y. Woon, and L. I, Phys. Rev. Lett. **93**, 220602 (2004).

[26] A. Melzer, A. Homann, and A. Piel, Phys. Rev. E **53**, 2757 (1996).

[27] V. Nosenko, S. K. Zhdanov, A. V. Ivlev, C. A. Knapek, and G. E. Morfill, Phys. Rev. Lett. **103**, 015001 (2009).

[28] P. Hartmann, A. Douglass, J. C. Reyes, L. S. Matthews, T. W. Hyde, A. Kovács, and Z. Donkó, Phys. Rev. Lett. **105**, 115004 (2010).

[29] B. Smith, T. Hyde, L. Matthews, J. Reay, M. Cook, and J. Schmoke, Adv. Space Res. **41**, 1510 (2008).

[30] Y.-J. Lai and L. I, Phys. Rev. Lett. **89**, 155002 (2002).

[31] T. Ott and M. Bonitz, Phys. Rev. Lett. **103**, 195001 (2009).

[32] J. D. Williams, E. Thomas, L. Couëdel, A. V. Ivlev, S. K. Zhdanov, V. Nosenko, H. M. Thomas, and G. E. Morfill, Phys. Rev. E **86**, 046401 (2012).

[33] V. Nosenko, S. Zhdanov, A. V. Ivlev, G. Morfill, J. Goree, and A. Piel, Phys. Rev. Lett. **100**, 025003 (2008).

[34] V. Nosenko, S. Zhdanov, and G. Morfill, Phys. Rev. Lett. **99**, 025002 (2007).

[35] V. Nosenko, A. V. Ivlev, and G. E. Morfill, Phys. Rev. Lett. **108**, 135005 (2012).

[36] P. Hartmann, A. Z. Kovács, A. M. Douglass, J. C. Reyes, L. S. Matthews, and T. W. Hyde, Phys. Rev. Lett. **113**, 025002 (2014).

[37] A. Melzer, V. A. Schweigert, and A. Piel, Phys. Rev. Lett. **83**, 3194 (1999).

[38] A. V. Ivlev, J. Bartnick, M. Heinen, C.-R. Du, V. Nosenko, and H. Löwen, Phys. Rev. X **5**, 011035 (2015).

[39] S. V. Vladimirov and M. Nambu, Phys. Rev. E **52**, R2172 (1995).

[40] M. Lampe, G. Joyce, G. Ganguli, and V. Gavrishchaka, Phys. Plasmas **7**, 3851 (2000).

[41] G. A. Hebner, M. E. Riley, and B. M. Marder, Phys. Rev. E **68**, 016403 (2003).

[42] R. Kompaneets, G. E. Morfill, and A. V. Ivlev, Phys. Rev. E **93**, 063201 (2016).

[43] A. V. Ivlev and G. Morfill, Phys. Rev. E **63**, 016409 (2000).

[44] S. K. Zhdanov, A. V. Ivlev, and G. E. Morfill, Phys. Plasmas **16**, 083706 (2009).
[45] L. Couëdel, S. K. Zhdanov, A. V. Ivlev, V. Nosenko, H. M. Thomas, and G. E. Morfill, Phys. Plasmas **18**, 083707 (2011).
[46] A. V. Ivlev, S. K. Zhdanov, M. Lampe, and G. E. Morfill, Phys. Rev. Lett. **113**, 135002 (2014).
[47] T. B. Röcker, L. Couëdel, S. K. Zhdanov, V. Nosenko, A. V. Ivlev, H. M. Thomas, and G. E. Morfill, Europhys. Lett. **106**, 45001 (2014).
[48] L. Couëdel, V. Nosenko, A. V. Ivlev, S. K. Zhdanov, H. M. Thomas, and G. E. Morfill, Phys. Rev. Lett. **104**, 195001 (2010).
[49] L. Couëdel, S. Zhdanov, V. Nosenko, A. V. Ivlev, H. M. Thomas, and G. E. Morfill, Phys. Rev. E **89**, 053108 (2014).
[50] S. S. Rogers, T. A. Waigh, X. Zhao, and J. R. Lu, Phys. Biol. **4**, 220 (2007).
[51] Y. Feng, J. Goree, and B. Liu, Rev. Sci. Instrum. **78**, 053704 (2007).
[52] See Supplemental Material at http://link.aps.org/supplemental/10.1103/PhysRevE.96.043201 for Movies S1 and S2.
[53] L. Couëdel, T. B. Röcker, S. K. Zhdanov, V. Nosenko, H. M. Thomas, and A. V. Ivlev, Europhys. Lett. **115**, 45002 (2016).
[54] M. T. Dove, *Introduction to Lattice Dynamics* (Cambridge University Press, Cambridge, UK, 1993).
[55] P. Hartmann, G. J. Kalman, Z. Donkó, and K. Kutasi, Phys. Rev. E **72**, 026409 (2005).
[56] N. P. Kryuchkov, S. A. Khrapak, and S. O. Yurchenko, J. Chem. Phys. **146**, 134702 (2017).